Desalination and Water Treatment
www.deswater.com

doi: 10.5004/dwt.2022.28941

277 (2022) 215–233
November

Comparative study on the removal of methyl orange using zeolite/biochar-supported iron oxide catalyst from industrial by-products

R. Ranjana*, R. Anjana, B. Sajeena Beevi

Department of Chemical Engineering, Government Engineering College Thrissur, Thrissur, APJ Abdul Kalam Technological University, Kerala, India, Tel. +91-9846035870; email: ranjana@gectcr.ac.in (R. Ranjana), Tel. +91-9446024544; email: anjana@gectcr.ac.in (R. Anjana); Tel. +91-9446317516; email: sajeenanazer@gmail.com (B. Sanjeena Beevi)

Received 31 May 2022; Accepted 21 September 2022

ABSTRACT

Biochar- and zeolite-supported iron oxide catalyst (BC-Fe and Z-Fe, respectively), were prepared from industrial by-products using a solvent-free method. The effectiveness of the prepared catalysts was tested by conducting batch experiments to remove methyl orange (MO) dye from dye-laden water. The optimum process variables for a maximum removal efficiency were identified using the Box–Behnken design of experiments (DoE) technique. The variables chosen were contact time, adsorbent dosage, pH, and initial adsorbate dosage. BC-Fe has a removal efficiency of 95% at a high acidic pH with a lower adsorbent concentration (3–5 g/L), as compared to that of the Z-Fe adsorbent (4–5 g/L). The higher surface area and pore volume of BC-Fe (66.998 m^2/g, 17 cc/g) than that of Z-Fe (50.039 m^2/g, 13.07 cc/g) resulted in a better removal efficiency with a low adsorbent dosage. Statistical verification was performed to check the real-time robustness of the developed Box–Behnken DoE model. The methyl orange (MO) dye adsorption was best described by the Langmuir, Freundlich and Temkin adsorption isotherms. Kinetic studies revealed that the pseudo-second-order kinetic model with rate constants of 0.01156 (BC-Fe) and 0.02063 g/mg·min (Z-Fe) was the best fit for adsorption. Thermodynamic studies revealed that the adsorption is spontaneous and endothermic with an increase in randomness at the solid–liquid interface.

Keywords: Biochar; Zeolite; Methyl orange; Slow pyrolysis

1. Introduction

Rapid industrialization has resulted in the generation of huge quantities of waste. The lack of proper segregation and processing of these wastes results in water and air pollution. The idea of converting waste to energy was developed earlier, and research to properly utilize these energy forms is progressing. Industries are generating large amounts of biomass waste, which are a good energy source that can be used in various applications. Waste-to-energy conversion is considered the most efficient method for reducing the pollutant load on water bodies, soil, and air. Biomass can be converted into carbonaceous forms for use as adsorbents and supports in various physical and chemical processes. Various studies have been conducted using C produced from biomass to remove pollutants, such as color, turbidity, heavy metals and their derivatives, and dyes, from chemical industry effluent water [1–5].

Methyl orange (MO) is a water-soluble acidic anionic azo dye used in the textile industry as a dye pigment, food industry, printing, paper manufacturing, pharmaceuticals, analytical chemistry laboratory experiments, and other commercial applications. It is mainly used in analytical chemistry laboratories as an acid–base indicator. MO can function as a weak acid when the aqueous solution has a pH of approximately 6.5 (5 g/L, H_2O, 20°C) [6], making it suitable for use as an acid–base indicator. Wastewater

* Corresponding author.

containing MO has a poor biochemical purification ability; thus, it is difficult to degrade. It is a threat to human health and damages the ecological balance owing to its carcinogenicity and mutagenicity [7]. Other health hazards include vomiting, breathing problems, and diarrhea [8]. Upon ingestion, it is metabolized to aromatic amines, which may lead to intestinal cancer [9,10]. The release of MO dye into water bodies reduces the penetration of sunlight into aquatic streams, which destroys aquatic plants and other organisms. Thus, it is necessary to develop an economical and efficient method for removing dye pigments from wastewater.

Various conventional methods include chemical and electrochemical methods [11], membrane separation [12], physical methods such as adsorption [2,3], and biological treatment methods. Adsorption is considered a simple, efficient, and cost-effective method, as compared to the other methods. High surface area and porosity are key elements to be considered when selecting an adsorbent for specific use [13]. Minerals, organic and inorganic materials such as activated clay minerals and C, industrial by-products, zeolite (Z), polymer materials, and metal oxides are commonly used adsorbents for the removal of pollutants from wastewater [4,13–17]. The major drawback of adsorption technology is the difficulty and cost of adsorbent regeneration after the specified purpose of removing pollutants from wastewater. This can be overcome by using industrial by-products, which is considered waste from the production unit, as raw materials for the adsorbent.

This study focuses on the use of industrial by-products, such as biomass from the Ayurveda industry and spent Z from the fluid catalytic cracking (FCC) unit of a petroleum refinery, for the support of metal oxides. Iron oxide, obtained as a by-product of an acid regeneration plant in the TiO_2 manufacturing industry, is used as a catalyst for the removal of MO from wastewater. Metal oxides and supports are thermally and mechanically derived from industrial by-products to enhance the sorption capacity of adsorbents. A supported catalyst was prepared using a two-step process. The first step included the production of a support for the metal oxide. The second-step included the incorporation of a metal oxide into the support using a planetary ball mill.

The raw material from the Ayurveda industry includes the roots of medicinal trees and shrubs for making "Dashamoola Kashayam" and "Dashamoola Arishtam". According to Ayurveda, "Dash" means ten and "moolam" are roots. The roots of trees include Kasmari (*Gmelina arborea*), Agnimantha (Premna mucronata and Premna integrifolia), Patala (Stereospermum suaveolens), Shyonaka (Oroxylum indicum), and Bilva (Aegle marmelos), and shrubs include Shalaparni (Desmodium gangeticum), Brihati (Solanum indicum), Kantakari (Solanum xanthocarpum), Gokhru (Tribulus terrestris), and Prishnaparni (Uraria picta). The health benefits of Dashmoola are numerous and are used as medicine for major issues, including arthritis, asthma, headache, puerperal problems, Parkinson's disease, gout, muscle spasm, and lower back ache. It can absorb almost all forms of toxicity in the human body. They are referred to as the best adsorbent combination available in nature according to the ancient medical science, Ayurveda [17].

The adsorptive properties of these roots alone or in combination have not yet been explored. After medicinal production, these roots are generally burned in open air. These waste materials were used as raw materials to produce biochar (BC). Even though adsorbents are considered a successful material for the removal of pollutants, raw adsorbents without any modification result in low sorption efficiencies. The sorption efficiency can be improved by surface modification through thermal treatment or by attaching chemical functional groups to the binding sites on the surface of the adsorbent [18–20]. Iron oxide was attached to the binding sites of the BC/regenerated Z to study the variations in the MO dye removal efficiency using these supports.

Liu et al. [21] found that metal oxides act as adsorbents and catalysts for the oxidation of MO dye. They concluded that the presence of metal oxides degrades MO dye in wastewater through oxidation in the presence of solar light. Makeswari and Saraswati [22] studied the photocatalytic degradation of methylene blue and MO dyes using a chitosan bimetal oxide composite and found that MO was highly degraded (74.05%) by the chitosan-bimetal oxide adsorbent. Saeed et al. also revealed the possibility of the photocatalytic and thermal degradation of MO dye using Co-ZnO and ZnO nanoparticles (NPs) catalysts, respectively [23,24]. Therefore, it appears to be feasible to combine adsorption with the catalytic degradation of MO dye from wastewater in the presence of heat/light or other energy forms. Thus, this paper focuses on a comparative study of the sorption/catalytic capacities of the developed composites, Z-Fe and BC-supported iron oxide (Z-Fe and BC-Fe, respectively), for the removal of MO dye from dye-laden water.

2. Material and methods

2.1. Reagents

The chemical reagents used in this study were of analytical grade, and distilled water was used for the preparation of MO dye solutions of different concentrations. The residual concentration of MO dye was determined using a UV spectrophotometer (HITACHI U-2900 UV-visible double beam spectrophotometer) at a wavelength of 506 nm for pH < 3 and 464 nm for pH > 4. Absorption at various concentrations was noted for the prepared stock solutions, and a calibration curve was plotted. The residual MO concentration was calculated from the calibration curve.

2.2. Synthesis of adsorbent

2.2.1. Synthesis of BC-Fe

Ayurvedic waste materials, such as solid residue from the medicine manufacturing unit, were collected from a nearby Ayurveda medicine manufacturing unit in Kerala. The waste material contained stems and roots of different plants obtained after the preparation of Dashmoola Kashayam/Arishtam. The wet sample was stirred for several weeks. After drying and grinding, the sample was sieved to a uniform size of 105 μm, which is less than the particle size range at which BC is produced. Studies were conducted using a particle size range of 0.2–2 mm [25]. The

literature does not agree on the effect of particle size on BC yield. Iron oxide (Fe_2O_3) from acid regeneration plants is one of the major wastes generated by the TiO_2 manufacturing industry. Fe_2O_3 was collected from a nearby TiO_2 manufacturing company. The collected Fe_2O_3 sample was a dark red dry powder.

BC from the collected biomass was prepared by slow pyrolysis in a tubular furnace. The tube used in the tubular furnace was made of quartz glass, had a length of 1,200 mm, and was purchased from HiTech Ceramics, Chennai. The outer and inner diameters of the tube was 50 and 45 mm, respectively. The biomass was heated to a maximum temperature of 500°C at a heating rate of 6°C/min for 3 h. A Nitrogen gas flow was maintained at 50 mL/min to provide an inert atmosphere inside the tubular furnace [25]. An increase in the gas flow rate beyond 50 mL/min reduces the vapor residence time inside the furnace and restricts the initiation of the repolymerization process, which results in a low BC yield.

Fe_2O_3 was incorporated into the BC using a planetary ball mill. The prepared BC (100 g) was placed in the jar of the planetary ball mill, 5% Fe_2O_3 (5 g) was added to the BC, and 200 g of zirconium balls were placed inside the jar. The planetary ball mill equipment was operated at 400 rpm for 2.5 h. The rotation direction was altered every 0.5 h to increase the efficiency of the ball mill. After the incorporation of Fe_2O_3 into the prepared BC sample, it was washed with deionized water to remove impurities. Washing was repeated three to five times to increase the purity of the prepared sample. The incorporated sample was dried overnight in an oven at 105°C to remove the moisture content present in the sample.

2.2.2. Synthesis of Z-Fe

The spent Z catalyst from the FCC unit of a nearby refinery, which was readily available in a 63 μm sieve size, was collected. The collected waste was oven-dried at 120°C. The Z catalyst was regenerated by mixing it with a mixture of acids at 10% concentration (acetic acid to oxalic acid weight ratio 1:1) in a magnetic stirrer at 45°C for 1.5 h. After acid treatment, the Z was separated by filtration and dried at 110°C in an oven [26]. Fe_2O_3 was incorporated into the pores of the regenerated Z by placing 500 g of regenerated Z, 25 g of Fe_2O_3 (5% of Z), and 1,000 g of zirconium balls in a jar. The samples were milled in a planetary ball mill at 400 rpm for 2.5 h.

2.3. Characterization of the adsorbents

The phase structure of the BC, prepared catalyst BC-Fe, and the regenerated Z and Z-Fe catalysts were studied using powder X-ray diffraction (XRD). The thermal stabilities of the prepared BC, Z, and composite catalysts were analyzed using thermogravimetric analysis (TGA). The weight loss of the prepared materials when subjected to heat was analyzed using a SDT Q600 V20.9. Fourier-transform infrared spectroscopy (FTIR) analyses of Z, Z-Fe, BC, and BC-Fe were conducted using an ALPHA II Compact FTIR spectrometer at the analytical instrument facility in Amrita Viswa Vidyapeedam, Coimbatore. The functional groups present in the prepared samples were analyzed using a spectrometer. The chemical composition and structural characteristics of the prepared materials were identified using scanning electron microscopy (SEM) images and energy-dispersive X-ray spectroscopy (EDS) analyses. The SEM-EDS image mapping of the prepared samples was performed using a ZEISS Gemini SEM 360 at the analytical instrument facility in Amrita Viswa Vidyapeedam, Coimbatore. The Brunauer–Emmett–Teller (BET) analysis of BC, BC-Fe, and Z-Fe was conducted at the analytical facility at the Center for Material for Electronics Technology (C-MET), Thrissur. The specific surface areas of the prepared BC and composite catalysts were calculated using the BET method based on Nitrogen adsorption/desorption isotherms measured at a bath temperature of 77 K in QuadraSorb Station 2 version 6.

2.4. Experimental methods

2.4.1. Statistical analysis

Batch experiments were conducted to study the effects of contact time, pH, initial MO concentration, and adsorbent dosage. The Box–Behnken method, design of experiment (DoE) technique, was used in this study to determine the optimum process variables to obtain the maximum removal efficiency. Minitab 16 software was used to generate combinations of process variables to optimize the variables affecting adsorption. In this study, four variables were selected, namely contact time, initial concentration of MO, initial adsorbent concentration, and pH. Three levels of contact time, initial concentration of MO dye, initial adsorbent concentration, and pH were selected based on the design table suggested by the Box–Behnken DoE method and are listed in Table 1.

The 27 combinations of variables were selected, and an adsorption study was conducted in all combinations with both supported catalysts. Table 4 presents the experimental results. The contact time was varied from 10 to 90 min, the initial concentration of MO dye from 20 to 200 ppm, the initial adsorbent dosage from 1 to 5 g/L, and the pH from 2 to 6. The removal efficiencies of the two adsorbents were determined using specified sets of process variables given by Minitab 16. Based on the regression analysis, the experimental results were used to fit the general mathematical model expression given by Eq. (1).

$$y = \beta_0 + \sum_{i=1}^{4}\beta_i x_i + \sum_{i=1}^{4}\beta_{ii} x_i^2 + \sum_{i<j=1}^{3}\beta_{ij} x_i x_j \quad (1)$$

Table 1
Variables used for the Box–Behnken design

Variables	Levels used, actual (coded)		
	Low (–1)	Medium (0)	High (1)
pH	2	4	6
Initial MO dye concentration	20	110	200
Initial absorbent concentration	1	3	5
Contact time	10	50	90

The quality of fit of the polynomial model equation was determined using R^2 and adjusted R^2 values. Statistical verification was performed to verify the robustness of the developed model in real-time situations. Regression coefficient estimation, *p*-tests, and ANOVA tests were performed for statistical verification with a 95% confidence level.

2.4.2. Adsorption isotherms

The adsorption isotherms were plotted after conducting batch adsorption studies which varied the initial MO dye concentration from 20–200 mg/L. All other parameters were obtained from the optimum results obtained by the response Surface Method (RSM) analysis. The equilibrium concentration of the MO dye was analyzed using a UV-visible double-beam spectrophotometer at a wavelength of 506 nm. The adsorbent capacity and removal efficiency under the optimized conditions (pH: 2, contact time: 60 min, adsorbent dosage: 4 g/L of Z-Fe and 3 g/L BC-Fe) were determined using Eqs. (2) and (3) at 30°C:

$$q_e = \frac{\left(C_0 - C_e\right) \times V}{m} \tag{2}$$

$$R = \frac{\left(C_0 - C_e\right) \times 100}{C_0} \tag{3}$$

where q_e is the equilibrium adsorption capacity (mg/g), R is the percentage removal efficiency, C_0 is the initial MO dye concentration (mg/L), C_e is the equilibrium MO dye concentration (mg/L), V is the volume of the solution (L), and m is the mass of the adsorbent (g).

The adsorption isotherm can be used to develop the relationship between the amount of dye adsorbed per unit mass of adsorbent and the amount of dye remaining in the solution after adsorption. Three adsorption isotherms, namely the Freundlich, Langmuir and Temkin isotherms were explored. Adsorption occurs on heterogeneous surfaces with unequal binding sites, and the surface energies are best described by the Freundlich isotherm [27]. The linear form of the Freundlich isotherm is given by Eq. (4):

$$\ln q_e = \ln K_f + \frac{1}{n} \ln C_e \tag{4}$$

where K_f and n are the Freundlich constants related to the adsorption capacity and adsorption intensity, respectively. The removal ability of the adsorbent over the concentration range of the dye solution is best described by the value of $1/n$. For highly concentrated dye solutions, the applicability of the adsorbent is ideal if the value of $1/n$ is >1. However, the applicability of the adsorbent for the entire range of dye solutions is possible when the value of $1/n$ is <1 [28].

The Langmuir isotherm is the best fit for monolayer adsorption. According to Langmuir, there are a fixed number of active binding sites on every adsorbent surface, and adsorption stops when these sites are occupied by the adsorbate. The model assumes that there is no transmigration of the adsorbate on the adsorbent surfaces, which have uniform energies [29]. The Langmuir isotherm is expressed as:

$$q_e = \frac{q_m K_L C_e}{1 + K_L C_e} \tag{5}$$

where q_m is the maximum monolayer coverage capacity (mg/g), and K_L is the Langmuir isotherm constant (L/mg).

The Langmuir isotherm defines a dimensionless constant or separation factor (R_L):

$$R_L = \frac{1}{1 + K_L C_0} \tag{6}$$

The value of R_L determines whether the adsorption is favorable [30]. An R_L value >1 indicates that the adsorption is unfavorable; R_L = 0 indicates irreversible adsorption, and R_L values between 0 and 1 indicate favorable adsorption. A straight-line plot of $1/q_e$ and $1/C_e$ indicates that the adsorption follows the Langmuir isotherm.

The Temkin adsorption isotherm considers the interaction between the adsorbate and the adsorbent. The Temkin adsorption isotherm refers to the adsorption on energetic and non-equivalent adsorption sites. It is assumed that the sites with high energy are first occupied by the adsorbate, and the heat of adsorption decreases linearly with the coverage of adsorbate over the adsorbent surface [31]. The linear form of the Temkin isotherm is expressed as:

$$q_e = B \ln K_T + B \ln C_e \tag{7}$$

where K_T is the Temkin isotherm equilibrium constant (L/g) and B is a constant related to the heat of adsorption (J/mol). The straight line plot of q_e and $\ln C_e$ indicates that the adsorption follows the Temkin isotherm. Table 8 lists the fitting results for all the isotherms.

2.4.3. Adsorption kinetics

Kinetic studies were conducted by taking samples at regular intervals ranging from 10 to 90 min at an adsorbent dose of 4 g/L of Z-Fe and 3 g/L of BC-Fe at a temperature of 30°C and pH of 2. The adsorbent dose, initial dye concentration, and pH were fixed according to the optimum results obtained from the RSM analysis. The amount of dye adsorbed on the adsorbent at equilibrium, q_e (mg/g), was calculated using Eq. (2). The amount of adsorption at time t, q_t (mg/g), was calculated using Eq. (8):

$$q_t = \frac{\left(C_0 - C_t\right) \times V}{m} \tag{8}$$

where C_0 and C_t (mg/L) are the liquid-phase concentrations of the dye initially and at time t, respectively, V is the volume of the solution (L), and m is the mass of the adsorbent (g).

The rate and mechanism of adsorption can be inferred from the kinetic data. To analyze the adsorption kinetics of MO dye using BC-Fe and Z-Fe, the pseudo-first-order, pseudo-second-order and intraparticle diffusion were tested. The fitting results are presented in Table 9.

A pseudo-first-order equation can be expressed in the linear form as:

$$\ln\left(q_e - q_t\right) = \ln q_e - \left(K_1 t\right) \tag{9}$$

where q_e and q_t are the amounts of MO dye adsorbed at equilibrium and time t (min), respectively, and k_1 is the rate constant of adsorption (min^{-1}). A linear plot of $\ln(q_e - q_t)$ vs. time was used to determine the rate constant k_1 [29].

The pseudo-second-order kinetic model describes the dependency of the adsorption capacity of the adsorbent on time and can be determined using on Eq. (10):

$$\frac{t}{q_t} = \frac{1}{k_2 q_e^2} + \frac{t}{q_e} \tag{10}$$

where q_t and q_e are the amounts of MO dye adsorbed at equilibrium and time t (min), respectively, and k_2 is the pseudo-second-order rate constant (g/mg·min). The linear plot of t/q_t against t was used to determine q_e and k_2 from the slope and intercept, respectively [15,32].

The intraparticle diffusion kinetic model was used to describe the diffusion-controlled liquid/solid adsorption kinetics [15]. The dependency of the adsorption capacity of the adsorbent on time can be determined using Eq. (11):

$$q_t = k_3 t^{0.5} + C \tag{11}$$

where k_3 is the intraparticle diffusion rate constant ($mg/g{\cdot}min^{1/2}$) and C is a constant related to the thickness of the boundary layer.

2.4.4. Thermodynamic studies

A thermodynamic study of the adsorption was conducted by varying the temperature of adsorption under the optimized process conditions obtained from the RSM analysis. The temperature was varied from 303–318 K. The equilibrium adsorption capacities of the adsorbent (q_e) were calculated at various temperatures. Thermodynamic parameters, such as the change in free energy (ΔG) (kJ/mol), enthalpy (ΔH) (kJ/mol), and entropy (ΔS) (J/mol·K) for the adsorption of the dye on the surfaces of the adsorbents can be calculated using Eqs. (12) and (13) [16]:

$$\frac{\ln q_e m}{C_e} = \frac{\Delta S}{R} - \frac{\Delta H}{RT} \tag{12}$$

$$\Delta G = \Delta H - T\Delta S \tag{13}$$

where m is the adsorbent dosage in mg/L.

The values of ΔH and ΔS are calculated from the slope and intercept of $\ln q_e m/C_e$ against the $1/T$ plot. The value of ΔG can be calculated using Eq. (13). The feasibility and spontaneity can be confirmed by the negative values of ΔG and positive values of ΔS. An increase in the absolute values of ΔG suggests that adsorption is favorable at higher temperatures [15,16]. The value of ΔH determines whether adsorption is endothermic or exothermic. The absolute value of ΔH determines whether the adsorption of the MO dye is physisorption or chemisorption [27]. Table 10 lists the thermodynamic parameters.

3. Results and discussion

3.1. XRD analysis

The phase structures of BC and the prepared supported catalyst (BC-Fe) were studied using powder XRD. Major peaks and reflections were identified between the 2θ values of 20° and 30°, indicating the high *C* content in the analyzed sample [33]. The cellulose in the plant residue contained in Ayurvedic by-products undergoes pyrolysis and is responsible for the peak at 2θ = 22.9°, and it shows a peak of 3.86 Å [34]. The diffraction peaks of BC at 20.77°, 21.74°, and 27.58° in Fig. 1a were attributed to the presence of quartz, sylvite, and calcite, respectively [35]. These results suggest that some inorganic phases were occluded within the *C* matrix of the BC. The BC XRD peaks exhibited a mixture of sharp peaks and broad humps for all 2θ values; thus, the BC can be defined as semi-amorphous. Fig. 1a also shows the XRD spectrum of BC-Fe. Two additional crystalline peaks, as compared to the XRD spectra of BC, were observed in the BC-Fe XRD spectra at 33.37° and 35.85° [35]. These peaks represent the Fe_2O_3 particles in the BC. The ash content and tarry materials trapped within the pores of the BC sample were responsible for the various sharp crystalline peaks in the XRD spectra of BC and BC-Fe [35]. It was found that BC-Fe was more crystalline than BC because the XRD spectra of BC-Fe had sharper peaks.

The XRD spectra of the spent Z after regeneration of the Z catalyst and Z with metal oxide incorporation were obtained. Fig. 1b compares the XRD patterns of spent Z and Z, confirming the removal of several metals via regeneration. Thus, it can be confirmed that the sample was regenerated using a mixed acid treatment [26]. The average crystallinity of the regenerated Z was similar to that of fresh Z [26]. An X-ray diffractogram was recorded at 2θ = 3°–79° with a chart speed of 0.001 min^{-1}. The peaks at 15.782° shown in Fig. 1b represents Al, which indicates that there was not much change in the structure. The peaks at 23.260° in Fig. 1b represent silica, indicating that there is no such change in the structure [36]. The peak at 34.915° [35] shown in Fig. 1b indicates the presence of Fe_2O_3 in the Z-Fe composite.

3.2. TGA analysis

A TGA analysis was conducted between 20°C–1,010°C at a heating rate of 10°C/min. Fig. 2 shows the graphs obtained from the TGA analysis of the BC, BC-Fe, Z, and Z-Fe samples. The TGA curves of the BC and BC-Fe samples showed an initial weight loss of 10% up to 100°C. This was due to the loss of moisture bound in the prepared BC and BC-Fe composite. The mass loss after 100°C in both samples is due to the decomposition and degradation of impurities, volatile matter, and *C* into CO, CO_2, and CH_4 [37]. The degradation of lignocellulosic fractions that did not decompose during pyrolysis was also responsible for the weight loss that occurred at 200°C–400°C [38].

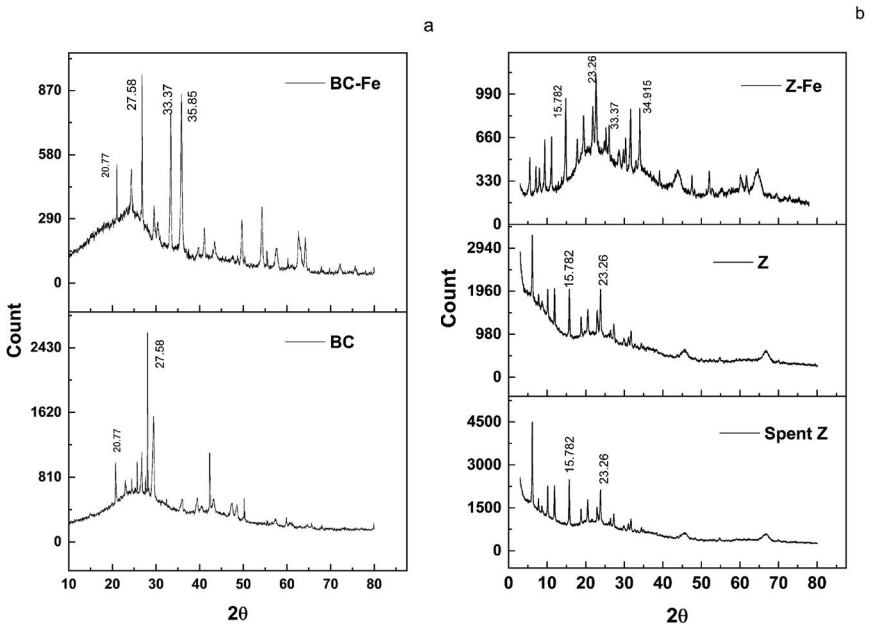

Fig. 1. XRD spectra of the adsorbents (a) BC and BC-Fe and (b) spent Z, Z, and Z-Fe.

The TGA curve of the regenerated Z in Fig. 2 shows that it was thermally stable. The TGA curve showed that the total mass loss was approximately 9.104%, which may be attributed to the loss of water in the Z. The TGA curve of Z-Fe in Fig. 2 shows that it was thermally stable and the total mass loss was approximately 12.54%, which was attributed to the loss of water in the Z. The two samples showed only a slight difference in their thermal stability. This result agrees with the results obtained by Salamaa et al. [39] in their study on the synthesis and characterization of Z and Z-encapsulated Fe compounds for the photocatalytic oxidation of direct blue-1 dye.

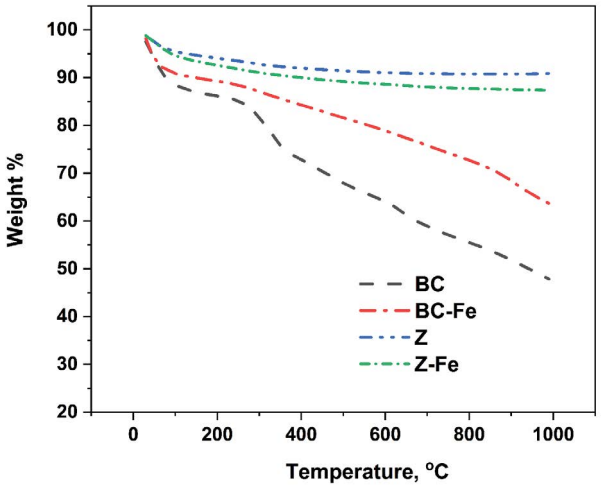

Fig. 2. TGA curves of BC, BC-Fe, Z, and Z-Fe.

3.3. FTIR analysis

Fig. 3a presents the FTIR spectra of BC and BC-Fe. Both spectra showed major peaks at 2,450–2,000; 3,700–3,000; 1,700–1,200 and 700–450 cm^{-1}. The broad peaks at 1,500 and 1,200 cm^{-1} indicate the presence of C=C bonds. The peaks at approximately 1,700–1,000 cm^{-1} represent the C–O groups in the sample. The peaks at approximately 1,000 cm^{-1} in the BC-Fe spectra are not clearly visible because of the removal of the C–O bond after the incorporation of Fe_2O_3. The peaks at 2,500–2,000 cm^{-1} indicate the C–C triple bond in the materials. Another major broad peak is visible in the FTIR spectra at approximately 3,500 cm^{-1}, and confirms the presence of O–H groups in the prepared BCs. It can be observed that the intensity of these peaks in the BC-Fe decreased, implying that the O–H groups were replaced by Fe after the incorporation of Fe_2O_3. Concurrently, the peaks representing the Fe–O bonds were strengthened after the incorporation of Fe_2O_3 (peaks at 600–450 cm^{-1}). A reduction in the weak peak centered at approximately 750 cm^{-1} was also observed, which indicates that some of the Si–O bonds in the BC were removed after the incorporation of Fe_2O_3. These results further support the findings obtained from the SEM-EDS analysis. The SEM-EDS results showed that there was a significant reduction in the concentration of silica after the modification of BC by the incorporation of Fe_2O_3.

Fig. 3b shows the FTIR spectra of the regenerated Z and Z-Fe. The FTIR spectrum of regenerated Z showed a large broad band at 1,080 cm^{-1} and another band at 455 cm^{-1}, which were attributed to the Al–O and Si–O functional groups, respectively. The FTIR spectrum only had bands corresponding to the Si–O and Al–O functional groups, indicating that the regeneration of the Z catalyst was successful. The FTIR spectra of Z-Fe showed a large broad band at 1,062 cm^{-1}, and other bands at 2,203; 2,030; 523, and 450 cm^{-1}. The band at 450 cm^{-1} represents the Si–O functional group, the band at 523 cm^{-1} represents the Fe–O functional group, and the large broad band at 1,062 cm^{-1} represents the Al–O functional

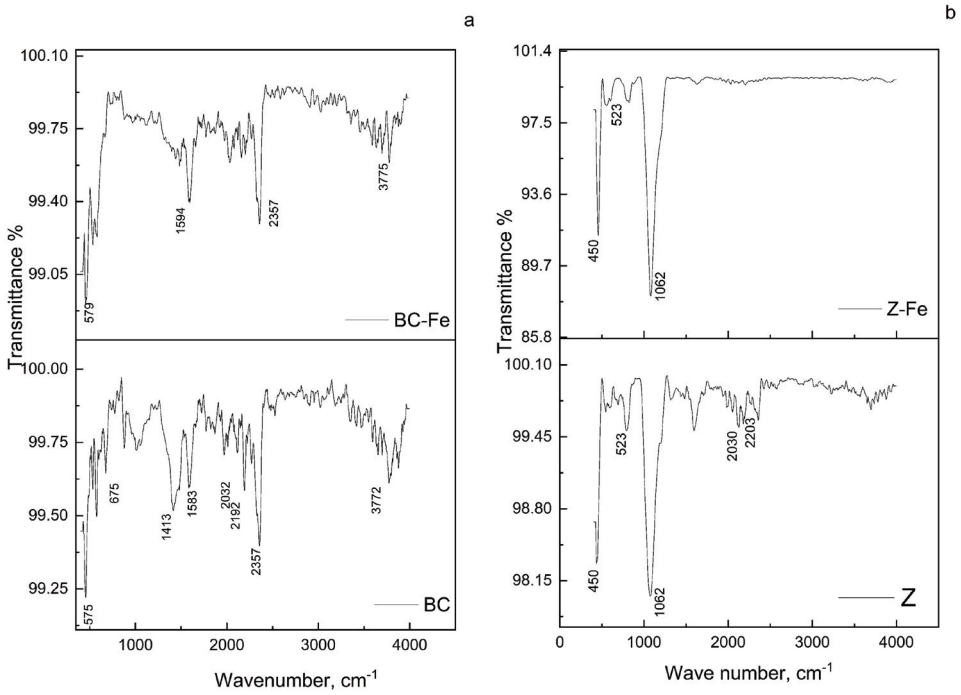

Fig. 3. FTIR spectra of (a) BC and BC-Fe and (b) Z and Z-Fe.

group. The presence of the Fe–O functional group confirms the incorporation of Fe_2O_3 into Z. These findings correspond with the findings published by Salamaa et al. [39].

3.4. SEM-EDS analysis

The chemical composition and structural characteristics of the prepared BC, Z and catalysts were identified using SEM images and EDS analyses. Fig. 4a presents SEM micrographs of the BC, which shows that BC had a porous structure and a smooth surface. This indicated that the prepared BC had an original morphological structure. It is clear that a heterogeneous and porous surface developed after pyrolysis [40]. Fig. 4b shows SEM images of the BC-Fe. Fig. 5 clearly shows that the surface of the BC-Fe composite was rough, and that Fe was distributed in the pores and surface of the BC. Iron particles can be clearly observed on the surface, confirming the successful incorporation of Fe. The SEM micrographs indicated that the prepared catalyst had a homogeneous distribution of Fe in the BC matrix.

Fig. 4c and d present the elemental spectra of the BC and BC-Fe samples, respectively, obtained using EDS. EDS detects X-rays from the samples excited by the highly focused and high-energy primary electron beams penetrating the sample. The elemental compositions of the prepared BC and BC-Fe were identified using EDS. From Fig. 4c, the major components of BC were C (47.9%) and O (28.1%). The other identified elements in the BC sample were Ca (10.7%), K (4.9%), Si (2.3%), Mg (1.5%), Al (1.3%), Cl (1.3%), P (1.2%), and Fe (0.8%). The content of Fe in BC was very low, as compared to that of other elements, before the incorporation of Fe_2O_3. The EDS spectrum of the BC-Fe sample (Fig. 4d) shows that the content of all elements, except C and Fe, decreased. The composition of Fe in the BC-Fe was 15%. The BC EDS spectrum showed a negligible Fe peak, indicating that Fe atoms were clearly incorporated in the BC-Fe sample. The Fe atoms replaced other elements, such as Mg, Al, Ca, K, and Cl, during the incorporation of Fe_2O_3. Therefore, the composition of these elements in BC-Fe decreased, as compared to the sample before incorporation. The SEM-EDS layered images of BC-Fe (Fig. 5) show that Fe atoms were distributed on the surface and pores of BC-Fe, confirming the fairly homogeneous incorporation of Fe_2O_3 in the prepared BC.

Fig. 6a–d show SEM-EDS images of the regenerated Z and Z-Fe. The observed size was in the range of nanometers at ×2,000 for Z and ×3,500 for Z-Fe. The particle size was reduced by milling, and the results showed an appropriate incorporation of Fe particles into the Z matrix.

3.5. BET surface area analysis

Fig. 7 shows the BET analysis results for the BC and BC-Fe samples. The figure shows that the surface area of BC was 38.052 m^2/g with a pore volume of 12.008 cc/g, and that of BC-Fe was 66.998 m^2/g, with a pore volume of 17 cc/g. BC-Fe exhibited a significantly larger surface area than BC. Notably, the total surface area of the BC-Fe increased after modification. A larger specific surface area indicates that the material has more adsorption sites. This indicates that the adsorption capacity of BC-Fe was greater than that of BC. The increase in the surface area of the BC after the incorporation of Fe_2O_3 may be due to the redox reactions between the Fe species and the BC C matrix. The formation of H_2O and CO_2 contributes to the development of microporosity [41]. The increase in the surface area of BC-Fe may

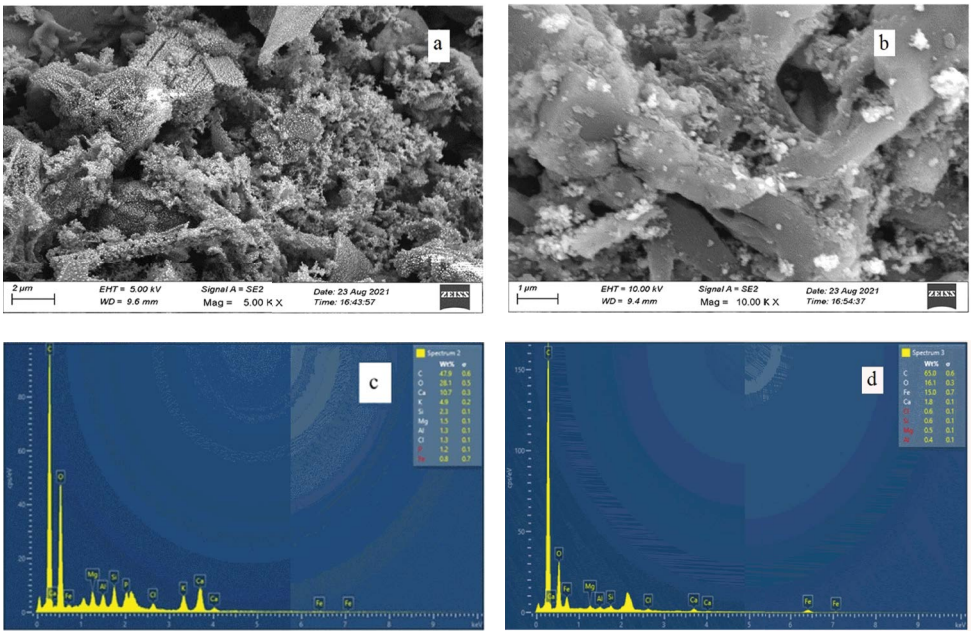

Fig. 4. SEM micrographs and EDS spectra of (a,c) BC and (b,d) BC-Fe.

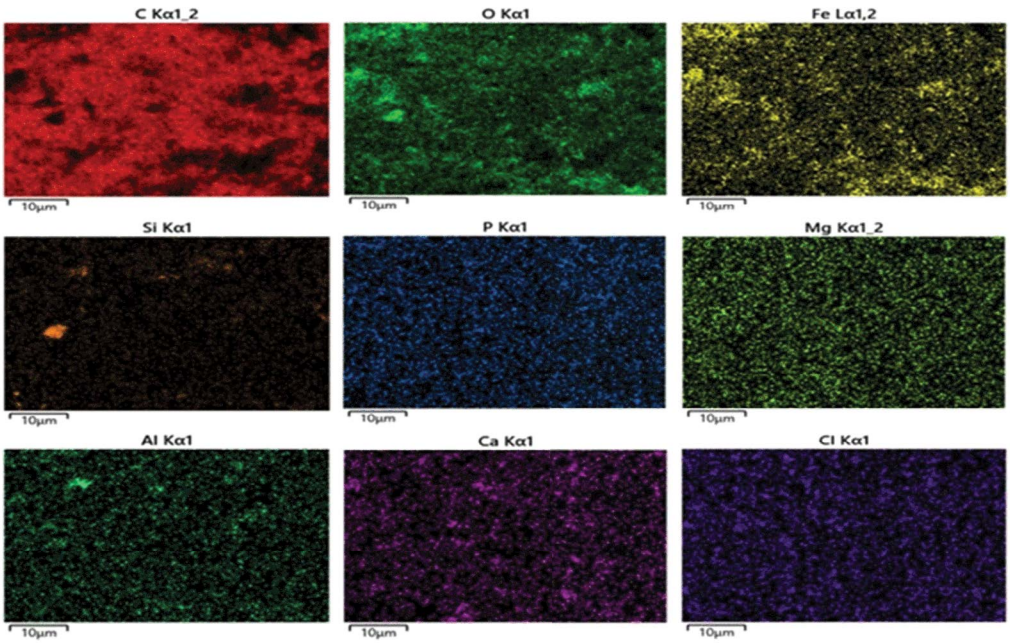

Fig. 5. SEM-EDS layered images of BC-Fe.

also be due to the ball milling during Fe_2O_3 incorporation. During ball milling, the Fe_2O_3 particles were crushed into the BC matrix and produced more pores. Consequently, the Fe_2O_3-incorporated samples exhibited a larger specific surface area than the raw BC sample [39,42]. Fig. 8 shows that the surface area of Z-Fe was 50.039 m^2/g. The large surface area indicated the presence of more pores, with a total pore volume of 13.07 cc/g. Table 2 lists the results of the BET surface area analysis. The surface area of Z-Fe was lower than that of the fresh Z catalyst, but it provided a sufficient surface area for the adsorption of MO dye [26].

3.6. Statistical analysis

The traditional optimization method does not show the combined effects of different input variables. Therefore, this study used RSM to optimize different variables and determine the combined effect of different input parameters [43,44]. Ozturk et al. [43] optimized the Cd^{2+} ion adsorption using pumice by varying the operating parameters, such as pH, initial adsorbate concentration, and temperature, using a central composite design. They developed a full quadratic model for Cd^{2+} ion adsorption. A similar

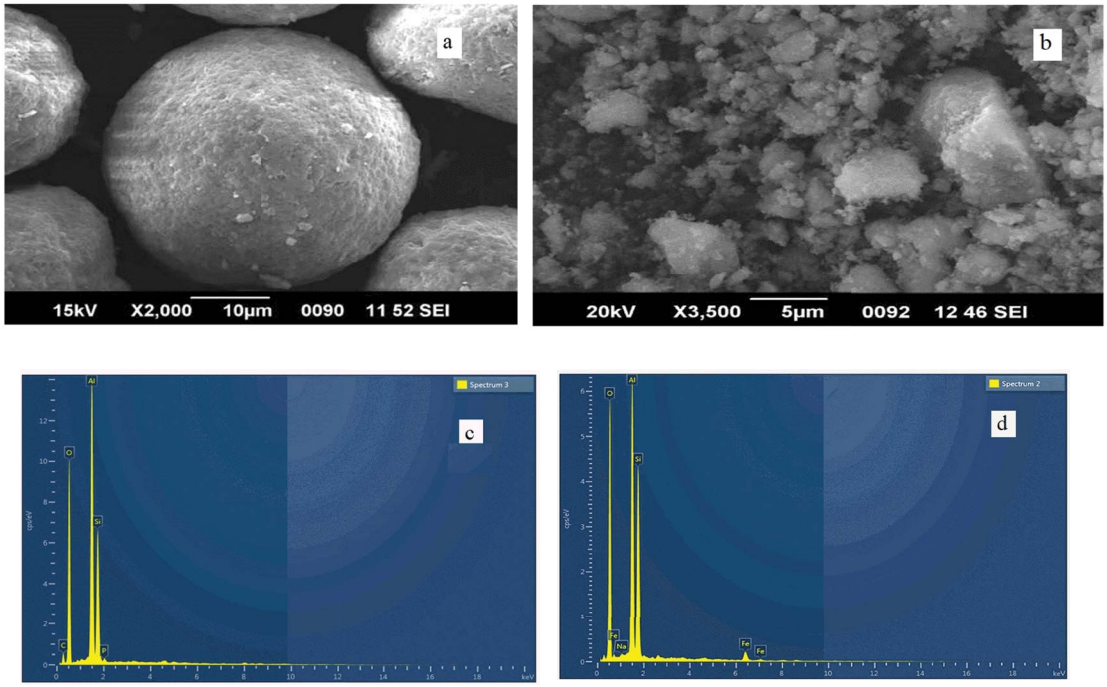

Fig. 6. SEM micrographs and EDS spectra of (a,c) Z and (b,d) Z-Fe.

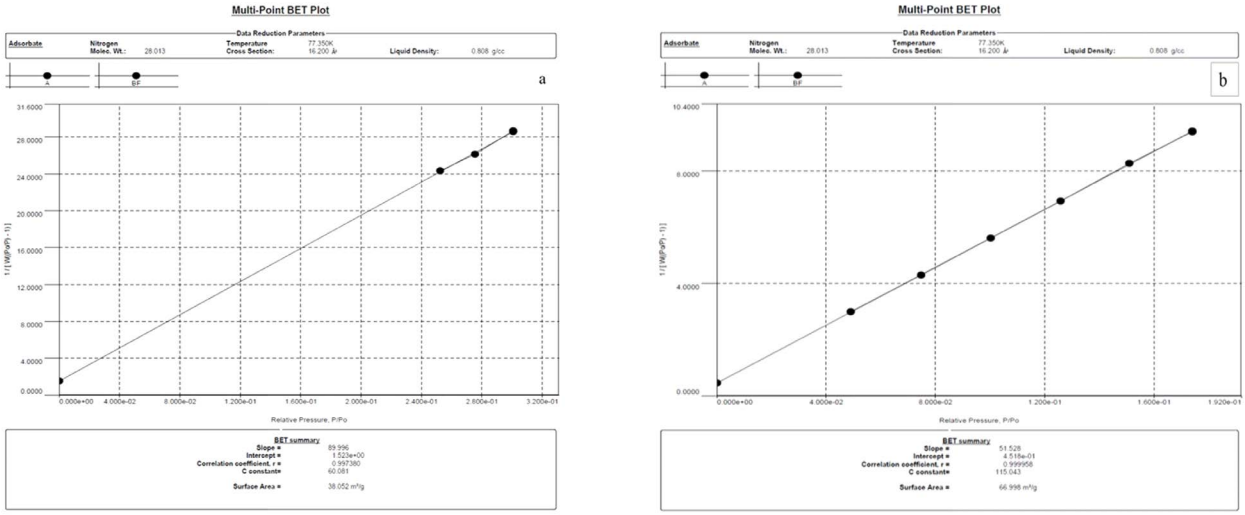

Fig. 7. Multi-point BET surface area analysis of (a) BC and (b) BC-Fe.

trend was observed in this study for the removal of MO dye using BC-Fe and Z-Fe. The results from the physical experiments show that all four variables affected the removal efficiency of both adsorbents, and a full quadratic model was fitted for MO dye adsorption.

Based on the regression analysis, the experimental results were used to fit the general mathematical model expression given in Table 3 for BC-Fe and Z-Fe, respectively.

Fig. 9 shows contour plots of the % removal efficiency of the prepared adsorbents under various process parameters. The contour and main effect plot shows that a removal efficiency of approximately 95% was possible at a very high acidic pH of approximately 2 with a contact time of 60–80 min using BC-Fe and Z-Fe [45,46]. These results agree with the findings of the adsorption study of Pb and MO dye removal using BC and BC-Fe by Tobias et al. [45].

From the adsorption study using the BC-Fe, an increase in contact time after 60 min had less effect on the removal of MO dye. A removal efficiency of approximately 95% was possible at low adsorbent concentrations for a contact time of approximately 60 min. This efficiency can be improved by increasing the adsorbent concentration, thereby reducing the contact time. However, for a cost-effective process, it is better to increase the contact time with a smaller amount of adsorbent. Additionally, to achieve 95% removal efficiency, less contact time is required for a small initial concentration

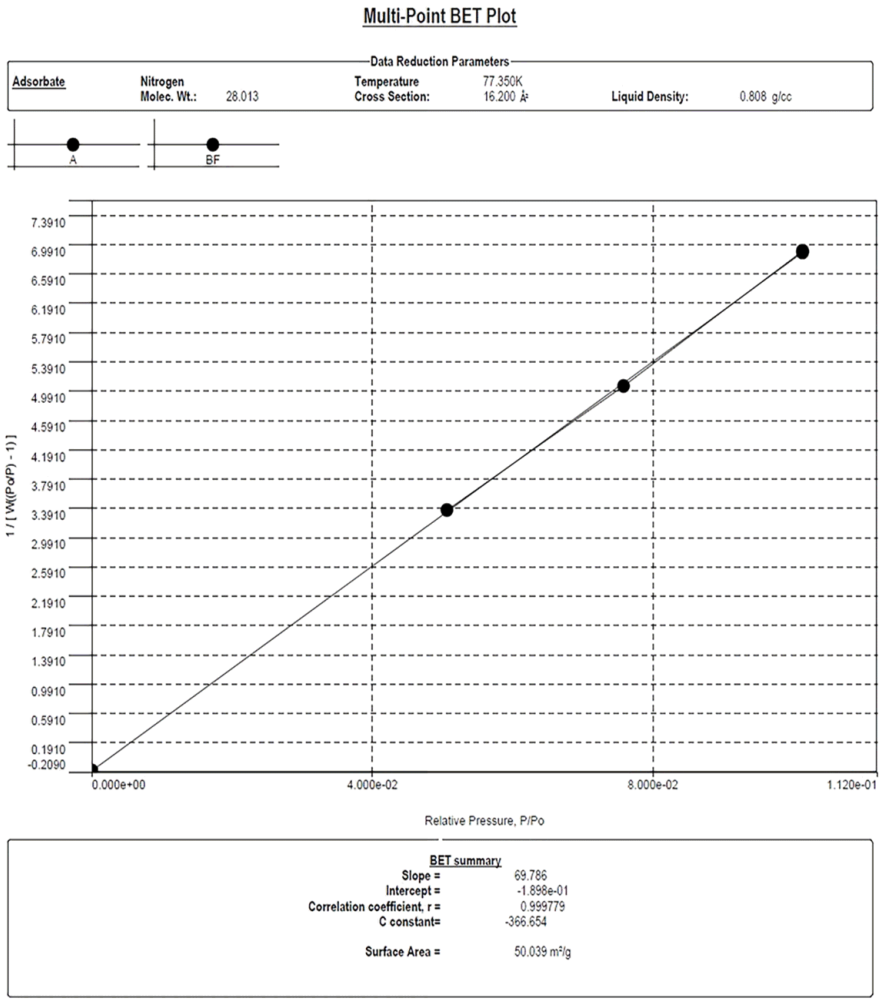

Fig. 8. Multi-point BET surface area analysis of Z-Fe.

Table 2
BET surface area and pore volume of the adsorbents

Sl. No.	Samples	Surface area (m^2/g)	Pore volume (cm^3/g)
1	BC	38.052	12.008
2	BC-Fe	66.998	17
3	Z-Fe	50.039	13.07

of adsorbate, and more contact time is required for a high initial MO dye concentration. The removal efficiency was high under highly acidic conditions. A 95% removal of MO dye was possible at approximately 3–5 g/L at a pH of 2–5. Above this pH level, the removal efficiency decreased to approximately 90%. Thus, the optimum value for 95% removal efficiency was at a concentration of 3 g/L of adsorbent at a pH of 2. There was not much interaction between the initial

Table 3
Regression analysis of BC-Fe and Z-Fe for the adsorption of MO

Material	Response	R^2 (%)	Adjusted R^2 (%)	Model equations in uncoded form
BC-Fe	% Removal efficiency	98.13	95.96	$96.6585 + 0.4878X_1 - 6.7940X_2 - 5.0661X_3 - 0.0263X_4 - 0.0037X_1^2 + 0.3838X_2^2 + 0.885X_3^2 + 0.0003X_4^2 + 0.0369X_1X_2 + 0.0092X_1X_3 - 0.0007X_1X_4 + 0.2292X_2X_3 - 0.0068X_2X_4 + 0.0014X_3X_4$
Z-Fe	% Removal efficiency	98.75	97.3	$91.69 + 0.5X_1 - 5.18X_2 - 3.61X_3 - 0.047X_4 - 0.0037X_1^2 + 0.1250X_2^2 + 0.656X_3^2 + 0.0003X_4^2 + 0.0344X_1X_2 + 0.0062X_1X_3 - 0.0006X_1X_4 + 0.25X_2X_3 - 0.0042X_2X_4 + 0.0014X_3X_4$

where X_1 is the contact time, X_2 is the pH, X_3 is the adsorbent concentration, and X_4 is the initial MO dye concentration. The R^2 and $R^2_{adj.}$ values of the response for both composite catalysts that were obtained at approximately 98% and 95% showed a very good fit with the experimental data using the RSM model.

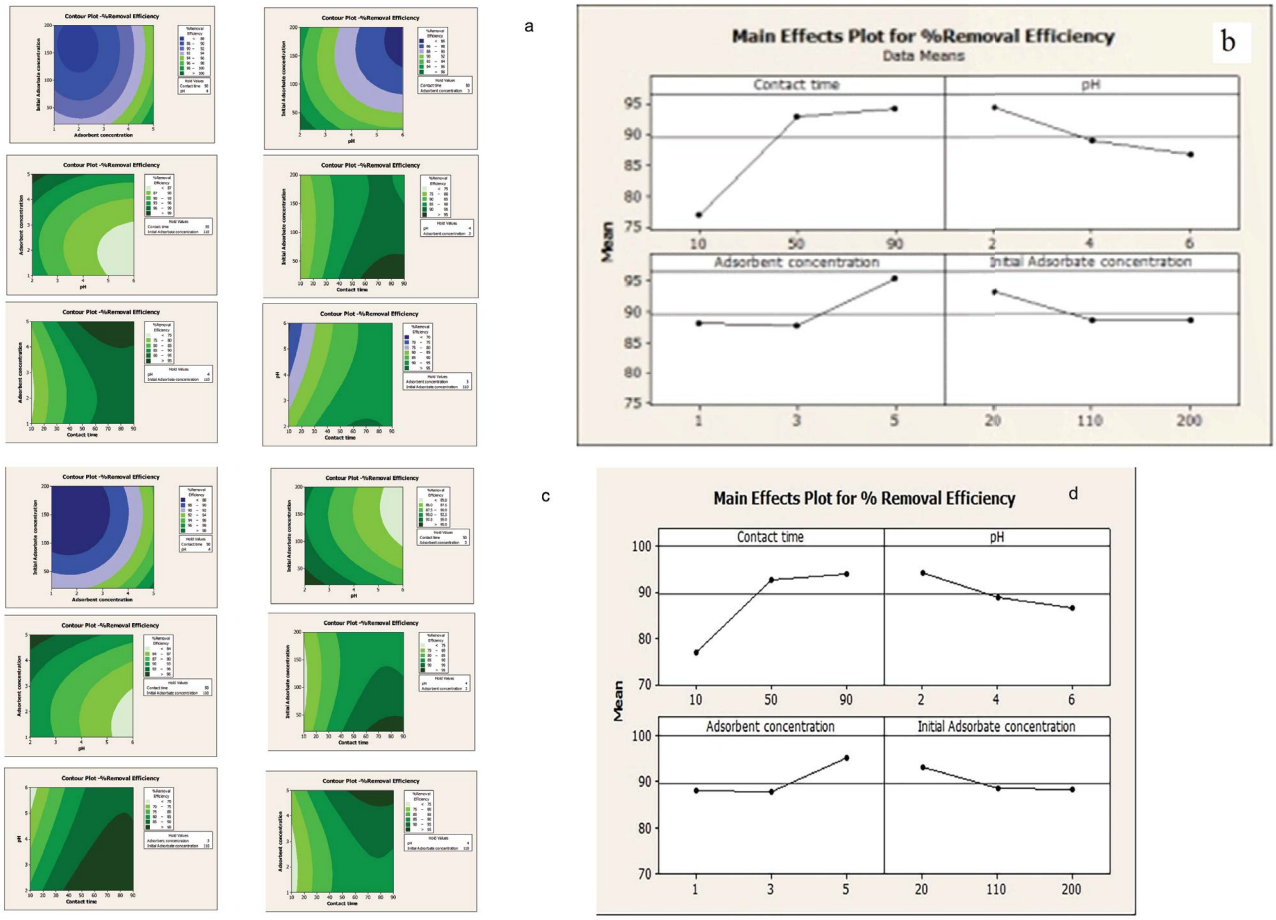

Fig. 9. Contour and main effect plot of the adsorption of MO dye using (a,b) BC-Fe and (c,d) Z-Fe.

MO dye concentration and pH value for the removal efficiency. Additionally, it was clear that the removal efficiency increased with the adsorbent concentration. The main effect plot supports the observations from the contour plot. Table 4 shows that the MO removal efficiency of the BC-Fe was higher than that of the Z-Fe for each combination of variables.

A similar trend was observed for the MO dye removal efficiency of Z-Fe. This trend can be attributed mainly to the small difference in surface area and the same affinity of the Fe particles towards the MO dye [45]. The MO removal efficiency was higher when using the BC-Fe than when using Z-Fe with a lower amount of adsorbent. This result shows the significance of the surface area of the adsorbents in the adsorption studies.

The contour plot of Z-Fe shows that a removal efficiency of 90%–95% is possible for a contact time of 40–90 min for a pH range of 2–5. If the pH is increased, the contact time also needs to be increased to obtain a 90%–95% MO dye removal efficiency. Thus, the contour plot shows that there is an interaction between variables, such as contact time and pH, for the removal of MO dye. Furthermore, a removal efficiency >95% was possible when the adsorbent concentration and contact time were increased. The higher the adsorbent concentration, the more sites and MO-Fe interactions are available for the adsorption of MO dye. Therefore, the contact time and adsorbent concentration also showed an interaction with the removal efficiency. removal efficiencies >95% could be achieved by increasing the contact time with a smaller amount of adsorbent. The removal efficiency decreased to 90% with an increase in the MO dye concentration. The contour plot shows a low significance of removal efficiency by increasing the adsorbent concentration rather than that of a decrease in pH. A removal efficiency of 90% is possible for the maximum adsorbate concentration at a pH of 3. The efficiency could be improved to 95% by lowering the pH and initial adsorbate concentration. The significance of the adsorbent concentration on the removal efficiency can be considered low for the Z-Fe, which can be clearly seen from the *P*-value and significance level of each process variable on the % removal efficiency given in Table 7. The main effect plot also agreed with the contour plot findings. The *P*-values for each process variable and their interaction, along with the significance level, are given in Table 5. From Table 5 it is clear that a significance level >95% or *P*-value < 0.05 has a significant influence on the removal efficiency of the adsorbents. Thus, the influence of process variables and their interactions on the removal efficiency can be determined from the *P*-values predicted by the software [47,48].

Table 4
Box–Behnken experimental design table with the experimental response values of BC-Fe and Z-Fe

Run no.	pH	Contact time	Initial adsorbent conc.	Initial MO dye conc.	% Removal efficiency – BC-Fe	Predicted % removal efficiency – BC-Fe	% Removal efficiency – Z-Fe	Predicted % removal efficiency – Z-Fe
1	2	10	3	110	83.538	82.793	81	83
2	2	90	3	110	95.189	94.139	93	96
3	6	10	3	110	68.235	69.147	66	69
4	6	90	3	110	91.705	92.312	89	93
5	4	50	1	20	93.000	93.693	91	93
6	4	50	5	20	100.000	100.373	98	99
7	4	50	1	200	89.000	88.489	87	91
8	4	50	5	200	97.000	96.168	95	97
9	4	10	3	20	75.000	76.414	75	82
10	4	90	3	20	99.000	98.669	98	99
11	4	10	3	200	75.000	76.710	75	80
12	4	90	3	200	89.000	88.965	89	92
13	2	50	1	110	96.000	95.284	94	97
14	6	50	1	110	84.966	85.715	82	85
15	2	50	5	110	100.000	100.630	98	94
16	6	50	5	110	92.633	94.727	90	93
17	4	10	1	110	76.269	75.136	74	77
18	4	90	1	110	90.000	90.918	88	83
19	4	10	5	110	83.000	80.842	81	79
20	4	90	5	110	99.678	99.570	97	94
21	2	50	3	20	97.178	97.664	97	94
22	6	50	3	20	95.000	92.364	92	95
23	2	50	3	200	94.000	95.396	92	95
24	6	50	3	200	86.951	85.224	84	88
25	4	50	3	110	89.000	89.000	88	93
26	4	50	3	110	89.000	89.000	88	93
27	4	50	3	110	89.000	89.000	88	93

Based on the variance analysis (ANOVA) test, the full quadratic model was found to be suitable for the % removal efficiency. Tables 6 and 7 present the ANOVA results for the % removal efficiency. The *P*-values of the regression, linear, and square terms for both adsorbents were <0.05, indicating that these terms are significant in the model. An insignificant lack of fit is desirable, as it indicates that anything left out of the model is not significant, so a model that fits can be developed.

3.7. Adsorption isotherms

Three adsorption isotherms (namely, the Langmuir, Freundlich, and Temkin isotherms) were plotted by calculating the equilibrium adsorption capacity (q_e) in mg/g and the equilibrium concentration of the MO dye (C_e) in mg/L for both adsorbents, as shown in Figs. 10–12, respectively.

Table 8 tabulates the parameters related to the three adsorption isotherms.

From Table 8, all the three isotherms Langmuir (R^2 = 0.9794 for BC-Fe and 0.989 for Z-Fe), Freundlich (R^2 = 0.9795 for BC-Fe and 0.9722 for Z-Fe) and Temkin isotherms (R^2 = 0.9976 for BC-Fe and 0.9991 for Z-Fe) were fitted well with high R^2 values. As per Langmuir adsorption isotherm monolayer adsorption is followed by BC-Fe and Z-Fe. The values of $1/n$ obtained from the linear plot of the Freundlich isotherm were 0.2212 and 0.2911 for BC-Fe and Z-Fe, respectively. Because the $1/n$ value is less than one, the developed composites can be applied to the entire range of dye solutions. Kaith et al. [28] found that the capture of methylene blue from industrial effluent using a $K_2Zn_3[Fe(CN)_6]2{\cdot}9H_2O$ NP-reinforced gum xanthanpsyllium hydrogel nanocomposite followed the Freundlich adsorption isotherm with a $1/n$ value of <1. This ensured that the developed adsorbent was applicable to the entire range of dye solutions.

From Table 8 it is clear that the highest R^2 value was obtained for the Temkin isotherms of both adsorbents. The Temkin constant (K_T) indicates the equilibrium binding constant for the maximum binding energy, and B is the heat of sorption for both composites. From the large value of R^2, it can be concluded that there is a strong interaction between the adsorbate and adsorbent molecules [31].

3.8. Adsorption kinetics

The adsorption kinetics of the MO dye onto the developed adsorbents were investigated using pseudo-first-order, pseudo-second-order, and intraparticle diffusion

Table 5
P-value and significance level of each process variable on the % removal efficiency

Term	BC-Fe		Z-Fe	
	P-value	Significance level	*P*-value	Significance level
Constant	0	100	0	100
X_1	0	100	0	100
X_2	0.002	>99	0.004	>99
X_3	0.008	>99	0.015	>99
X_4	0.046	>95	0.102	>89
X_1X_1	0	100	0	100
X_2X_2	0.05	95	0.413	>59
X_3X_3	0	100	0.001	>99
X_4X_4	0.013	>98	0.002	>99
X_1X_2	0.004	>99	0.002	>99
X_1X_3	0.4	60	0.477	>50
X_1X_4	0.012	>98	0.006	>99
X_2X_3	0.299	>71	0.168	>83
X_2X_4	0.175	>82	0.292	>70
X_3X_4	0.772	>30	0.720	>29

Table 6
Variance analysis for the % removal efficiency of BC-Fe

Source	DF	Seq. SS	Adj. SS	Adj. MS	*F*	*P*
Regression	14	1,801.35	1,801.35	128.668	45.10	0
Linear	4	1,293.78	266.72	66.681	23.37	0
Square	4	435.94	435.94	108.985	38.20	0
Interaction	6	71.63	71.63	11.939	4.18	0.017
Residual error	12	34.23	34.23	2.853	–	–
Lack of fit	10	34.23	34.23	3.423	–	–
Pure error	2	0	0	0	–	–
Total	26					

where DF is the degrees of freedom of the terms used, Seq. SS is the sequential sum of squares of the terms used, Adj. SS is the adjusted sum of squares of all the terms, Adj. MS is the adjusted mean squares of the terms, *F* and *P*-value is the test statistic used to determine whether the model is missing higher-order terms that include the predictors in the current model.

kinetic models. Figs. 13–15 show the linear plots of all kinetic models and Table 9 lists the parameters corresponding to the kinetic model.

From the above plots, the R^2 value was high for the pseudo-second-order kinetic model (0.9998 for both BC-Fe and Z-Fe). The R^2 value was close to unity for the pseudo-second-order kinetic model [27]. Mittal et al. [27] found that the adsorption of an anionic dye (Congo red) follows pseudo-second-order kinetics with an R^2 value close to unity (0.99). This indicates that the pseudo-second-order kinetic model with rate constants of 0.01556 g/mg·min (BC-Fe) and 0.02063 g/mg·min (Z-Fe) was the best fit for this study. The pseudo-second-order kinetic model assumes that the rate-limiting step is chemisorption and predicts the behavior over the entire range of adsorption. Under these conditions, the adsorption rate depends on the adsorption capacity and not on the concentration of the adsorbate [49].

Table 7
Variance analysis for the % removal efficiency of Z-Fe

Source	DF	Seq. SS	Adj. SS	Adj. MS	*F*	*P*
Regression	14	1,764	1,764.42	126.03	67.97	0
Linear	4	1,316.5	235.65	58.9	31.77	0
Square	4	389.9	389.92	97.48	52.57	0
Interaction	6	58	58	9.67	5.21	0.007
Residual error	12	22.25	22.25	1.854	–	–
Lack of fit	10	22.25	22.25	2.225	–	–
Pure error	2	0	0	0	–	–
Total	26					

where DF is the degrees of freedom of the terms used, Seq. SS is the sequential sum of squares of the terms used, Adj. SS is the adjusted sum of squares of all the terms, Adj. MS is the adjusted mean squares of the terms, *F* and *P*-value is the test statistic used to determine whether the model is missing higher-order terms that include the predictors in the current model.

Table 8
Isotherm parameters of MO dye adsorption using BC-Fe and Z-Fe

Isotherms	Adsorbents	Parameters	Value	R^2
Langmuir	BC-Fe	q_m (mg/g)	33	0.9794
		K_L (L/mg)	14.2	
		R_L	0.0011	
	Z-Fe	q_m (mg/g)	34.6	0.989
		K_L (L/mg)	1.405	
		R_L	0.0084	
Freundlich	BC-Fe	K_f (mg/g·(mg/L)$^{-1/n}$)	25.028	0.9795
		$1/n$	0.2212	
	Z-Fe	K_f (mg/g·(mg/L)$^{-1/n}$)	20.697	0.9722
		$1/n$	0.2911	
Temkin	BC-Fe	K_T (L/mg)	420.502	0.9976
		B (J/mol)	4.6272	
	Z-Fe	K_T (L/mg)	51.49	0.9991
		B (J/mol)	6.069	

3.9. Thermodynamic studies

The effect of temperature on the adsorption process was studied by varying the temperature from 303–318 K under the optimum conditions obtained using RSM analysis. From Fig. 16, it was clear that an increase in temperature increased the adsorption capacity of both adsorbents. This indicated that the adsorption was endothermic (ΔH– +ve) for the selected temperature range. By evaluating the thermodynamic parameters, it was possible to ensure the spontaneity of the adsorption process using Eqs. (12) and (13). The values of ΔH and ΔS were calculated from

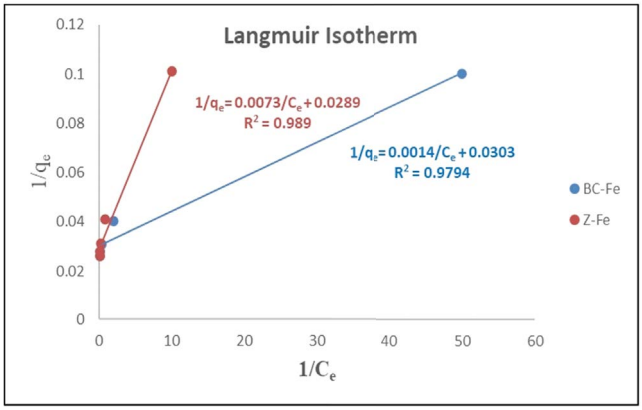

Fig. 10. Linear plot for the Langmuir adsorption isotherm of BC-Fe and Z-Fe.

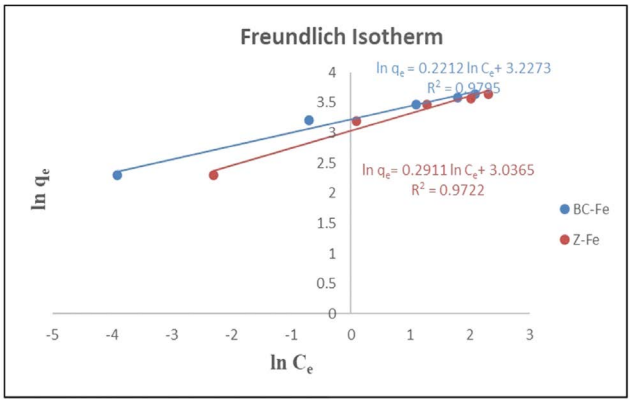

Fig. 11. Linear plot for the Freundlich adsorption isotherm of BC-Fe and Z-Fe.

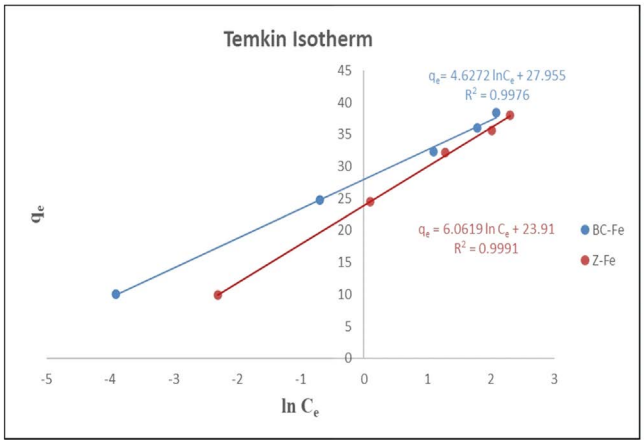

Fig. 12. Linear plot for the Temkin adsorption isotherm of BC-Fe and Z-Fe.

the slope and intercept of $\ln q_e m/C_e$ against the $1/T$ plot given in Fig. 17. The value of ΔG can be calculated using Eq. (13). Table 10 lists the thermodynamic parameters.

The positive values of the calculated ΔS indicate an increase in randomness at the solid-solution interface

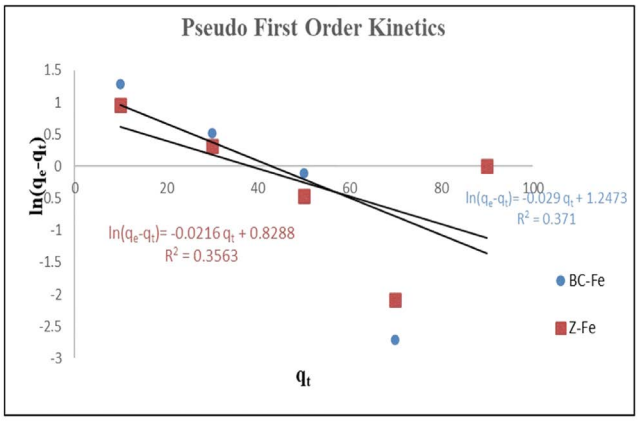

Fig. 13. Linear plot for the pseudo-first-order model.

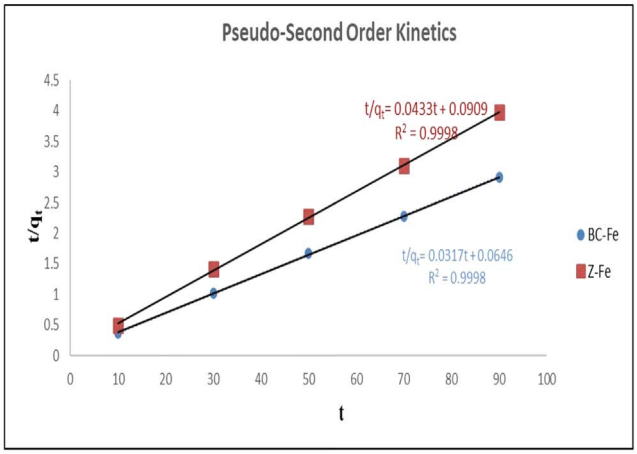

Fig. 14. Linear plot for the pseudo-second-order model.

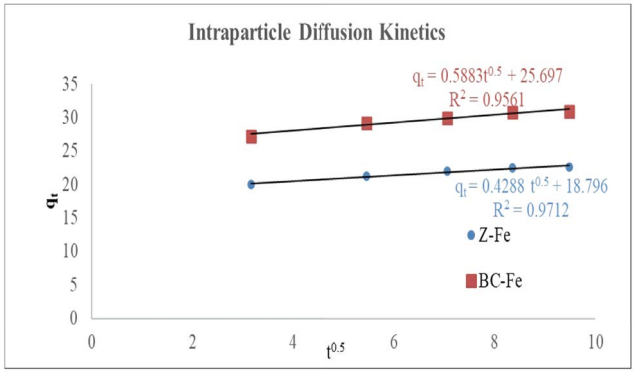

Fig. 15. Linear plot for the intraparticle diffusion model.

during adsorption. Feasibility and spontaneity were confirmed by the negative ΔG values and the positive ΔS values, respectively. The increase in the absolute values of ΔG with increasing temperature indicates that adsorption is favorable at higher temperatures [15,16]. The value of ΔH determines whether adsorption is endothermic or exothermic. The high absolute values of ΔH reveal that the adsorption

Table 9
Pseudo-first-order, pseudo-second-order, and intraparticle diffusion model constants and correlation coefficients for MO dye adsorption onto BC-Fe and Z-Fe

Kinetic model	Adsorbents	Parameters	Value	R^2
Pseudo-first-order	BC-Fe	k_1 (min^{-1})	–0.029	0.371
		q_e (mg/g)	17.67258178	
	Z-Fe	k_1 (min^{-1})	–0.0216	0.3563
		q_e (mg/g)	6.74	
Pseudo-second-order	BC-Fe	k_2 (g/mg·min)	0.015555614	0.9998
		q_e (mg/g)	31.54574132	
	Z-Fe	k_2 (g/mg·min)	0.020625832	0.9998
		q_e (mg/g)	23.09468822	
Intraparticle diffusion	BC-Fe	k_3 (mg/g·min$^{1/2}$)	0.5883	0.9561
		C	25.697	
	Z-Fe	k_3 (mg/g·min$^{1/2}$)	0.4288	0.9712
		C	18.796	

Table 10
Thermodynamic parameters for the adsorption of MO dye on BC-Fe and Z-Fe

Dye concentration	Adsorbents	ΔH	ΔS	ΔG (kJ/mol) at temperatures			
(mg/L)		(kJ/mol)	(kJ/mol·K)	303 K	308 K	313 K	318 K
100	BC-Fe	111.657	0.387	–5,813.09	–7,751.54	–9,689.99	–11,628.4
100	Z-Fe	67.118	0.239	–5,455.87	–6,653.46	–7,851.05	–9,048.64

Table 11
Comparison of the adsorption efficiency and capacity of other adsorbents with BC-Fe and Z-Fe for the removal MO dye

Adsorbent	% Removal efficiency	Adsorption capacity (mg/g)	References
Activated C from popcorn	48.5	969	[50]
Activated C from waste tire rubber	80	588	
BC from chicken manure	100	41.99	
Magnetic lignin-based C NPs	90.7	113	
α-Fe_2O_3 NPs	90	28.9	
ZIF-67 nanostructure	70.2	75.59	
BC	85	28.33	This study
Z	68	17	
Z-Fe	95	23.75	
BC-Fe	95	31.67	

of the MO dye is chemisorption [27]. This result agrees with the results obtained by Mittal et al. [27] for the adsorption of anionic dyes using bottom ash and de-oiled soya. The heat of adsorption was >40 kJ/mol using the adsorbent de-oiled soya (ΔH = 56.429 kJ/mol), which favors chemisorption.

4. Comparison of the adsorption of MO dye by BC-Fe and Z-Fe with other adsorbents

The dye uptake capacities of the developed BC-Fe and Z-Fe were compared with those of Z, BC, and other adsorbents reported in the literature [50]. The removal efficiencies of Z and BC were determined under the optimum conditions given by the RSM analysis (pH = 2, contact time = 60 min, initial MO dye concentration = 100 ppm, and initial adsorbent dosages of 3 g/L for BC and BC-Fe and 4 g/L for Z and Z-Fe). Table 11 lists the reported removal efficiency and adsorbent capacity of the developed supports and composites. The composites exhibited a reasonable adsorption capacity, as compared to other developed adsorbents. The data in Table 11 indicates that the incorporation of Fe_2O_3 increases the removal efficiency, even though the absorbent capacity is less than that of the other adsorbents. Additionally, by comparing the UV absorption spectra of the

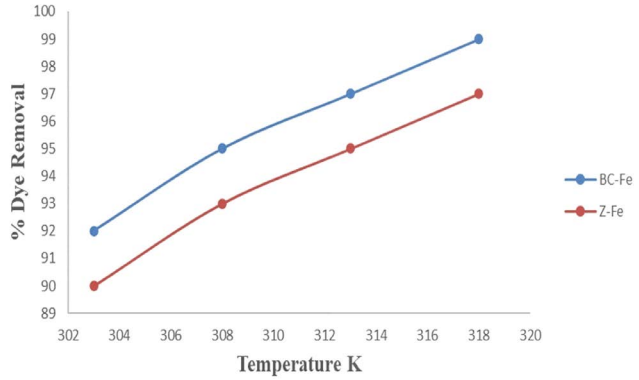

Fig. 16. Effect of temperature on dye removal using BC-Fe and Z-Fe composites.

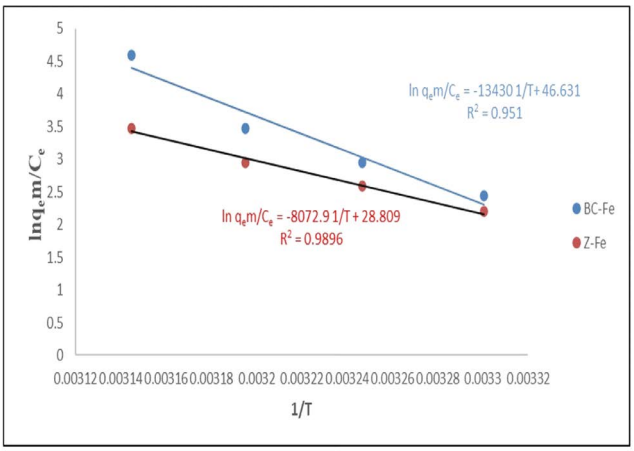

Fig. 17. Plot of $\ln q_e m/C_e$ vs. $1/T$ for BC-Fe and Z-Fe.

as-prepared and degraded MO solutions shown in Fig. 18, it was observed that the height of the absorption peak at 506 nm was drastically reduced. A shift of the 271 nm peak to 254 nm indicates that the –N=N– bond was completely decomposed, corresponding to the disappearance of the orange color in the solution, and a new benzene ring was formed with a smaller molecular weight as a reaction product after the degradation reaction [51]. This reveals that the MO dye was not only adsorbed to the sites of the composites but also degraded, resulting in a higher removal efficiency.

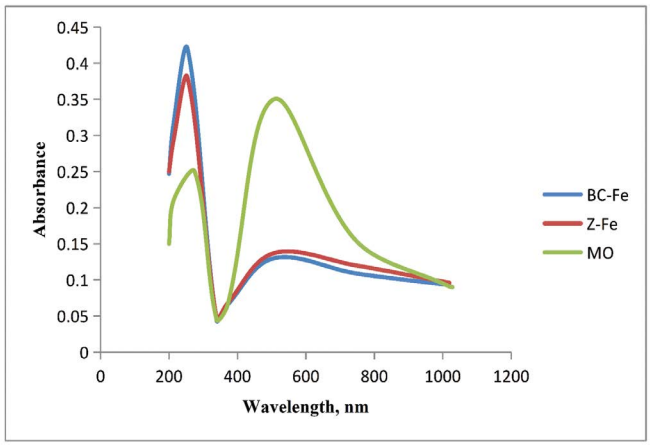

Fig. 18. UV-visible absorption spectra for the as-prepared and degraded MO solution using BC-Fe and Z-Fe.

5. Economic appraisal

Biomass, spent Z, and Fe_2O_3 were collected from nearby industries at no cost; however, collection and transportation costs need to be considered. However, the total cost of these composites is lower than that of commercially available activated C, Zs, and catalysts. Therefore, the regeneration and recovery of these may not be cost effective. Some means of chemical fixation, such as fire bricks and fillers in cement, can be used to dispose of these composites. A rough assessment of the capital cost of these composites for the removal of MO dye was made without considering the regeneration and disposal costs of these materials. This analysis considered only the saturation capacities of the composites. Using the saturation capacity values of various available adsorbents, the relative cost of the adsorbent for adsorbing 1 g of MO dye was calculated. This procedure has been followed by numerous researchers to calculate the adsorption cost [49,52–54]. Table 12 presents the economic cost and adsorption capacity of MO dyes for various adsorbents.

6. Conclusions

A comparative study on the MO dye removal efficiency of BC-Fe and Z-Fe derived from industrial by-products was performed. The effects of various operating parameters, such as contact time, pH, adsorbent dosage, and initial adsorbate dosage, on the removal efficiency were

Table 12
Cost and adsorption capacity of BC-Fe and Z-Fe, as compared to other adsorbents, for the adsorption of MO dye

Adsorbent	Adsorption capacity	Price/g of adsorbent as compared to BC-Fe price	Price/adsorbed gram of MO as compared to BC-Fe price	References
BC-Fe	31.67	1	1	This study
Z-Fe	23.75	0.75	1	This study
Chitosan/rectorite/carbon nanotubes	50.75	17.08	10.65	[55]
Fe_3O_4/CNTs	2.760	15.5	177.85	[56]

studied. The Box–Behnken – DoE technique was used in this study to determine the optimum process variables to obtain the maximum removal efficiency. It was observed from the investigations that all variables influenced the MO dye removal efficiency. MO removal was significantly influenced by the pH of the water. A highly acidic pH favors the removal of MO, with a removal efficiency >95%. The optimum conditions for the maximum removal efficiency for BC-Fe were found to be a pH of 2, contact time of 60 s, and adsorbent concentration of approximately 3–5 g/L for a maximum adsorbate dosage of 100 mg/L [46]. The optimum conditions for the maximum removal of MO dye using the Z-Fe composite was found to be a contact time of 40 s with an adsorbent dosage of approximately 4–5 g/L at a high acidic pH. This can be justified by the results obtained from the BET surface area analysis of both derived materials. The surface area of BC-Fe was 66.998 m^2/g with a pore volume of 17 cc/g which is greater than that of the surface area (50.039 m^2/g) and pore volume (13.07 cc/g) of Z-Fe. This resulted in a better dye removal efficiency with a lower concentration of BC-Fe than that of Z-Fe. Langmuir, Freundlich and Temkin isotherms were fitted to describe the equilibrium of the adsorption process. The removal of the MO dye followed pseudo-second-order kinetics. This revealed that the MO dye was chemically adsorbed onto the surfaces of BC-Fe and Z-Fe. The thermodynamic parameters ΔH, ΔS, and ΔG were calculated. The positive values of ΔH and ΔS revealed that adsorption was endothermic and random in nature. Because ΔH was >40 kJ/mol, adsorption proceeded via chemisorption. The negative values of the change in free energy showed that the adsorption was spontaneous, and its magnitude increased with temperature. Thus, it can be concluded that the presence of metal oxides significantly affect the rate of MO dye removal from dye-laden water. The future scope of this study includes scaling up to a pilot plant study to establish the efficacy of the derived composite adsorbents, regeneration capacity, evaluation of the residual concentration in the treated water, and removal efficiency with different dyes.

Symbols

β_0 — Constant term of mathematical model equation
β_i — Coefficient of linear terms of variables in mathematical model equation
x_i — Linear terms of variables in the mathematical model equation
β_{ii} — Coefficient of square terms of variables in the mathematical model equation
x_i^2 — Square terms of variables in the mathematical model equation
β_{ij} — Coefficients of the interaction terms of variables in the mathematical model equation
$x_i x_j$ — Interaction terms of the variables in the mathematical model equation
q_e — Equilibrium adsorption capacity, mg/g
R — Percentage removal efficiency, %
C_0 — Initial MO dye concentration in solution, mg/L
C_t — Liquid-phase concentrations of the dye at time t, mg/L
C_e — Equilibrium MO dye concentration, mg/L
V — Volume of the solution, L
m — mass of the adsorbent, g
K_f, n — Freundlich constants
q_m — Maximum monolayer coverage capacity, mg/g
K_L — Langmuir isotherm constant, L/mg
R_L — Separation factor
K_T — Temkin isotherm equilibrium constant, L/g
B — Constant related to the heat of adsorption, J/mol
q_t — Amounts of MO dye adsorbed at time t, mg/g
k_1 — Pseudo-first-order rate constant, min^{-1}
k_2 — Pseudo-second-order rate constant, g/mg·min
k_3 — Intraparticle diffusion rate constant, $mg/g \cdot min^{1/2}$
C — Constant related to the thickness of the boundary layer
ΔG — Change in free energy, kJ/mol
ΔH — Change in enthalpy, kJ/mol
ΔS — Change in entropy, J/mol·K

Funding sources

This study was supported by the TEQIP four funds, Government Engineering College, Thrissur, APJ Abdul Kalam Technological University.

Acknowledgement

This manuscript was edited by Editage-a brand of Cactus communications.

Declaration of competing interest

The authors declare that they have no known competing financial interests or personal relationships that could have influenced the work reported in this study.

References

[1] Z. Bencheqroun, I. El Mrabet, M. Nawdali, M. Benali, H. Zaitan, Adsorption removal of cationic dyes from aqueous solutions by raw and chemically activated cedar sawdust, Desal. Water Treat., 240 (2021) 177–190.
[2] Y. Abrouki, J. Mabrouki, A. Anouzla, S.K. Rifi, Y. Zahiri, S. Nehhal, A. El Yadini, R. Slimani, S. El Hajjaji, H. Loukili, S. Souabi, Optimization and modeling of a fixed-bed biosorption of textile dye using agricultural biomass from the Moroccan Sahara, Desal. Water Treat., 240 (2021) 144–151.
[3] R. Subramaniam, S.K. Ponnusamy, Novel adsorbent from agricultural waste (cashew NUT shell) for methylene blue dye removal: optimization by response surface methodology, Water Resour. Ind., 11 (2015) 64–70.
[4] S. Papirio, L. Frunzo, M. Rosaria Mattei, A. Ferraro, M. Race, B. D'Acunto, F. Pirozzi, G. Esposito, Sustainable Heavy Metal Remediation, E.R. Rene, E. Sahinkaya, A. Lewis, P.N.L. Lens, Eds., Environmental Chemistry for a Sustainable World, Springer, Berlin, 2017, pp. 25–64.
[5] A. Patel, S. Soni, J. Mittal, A. Mittal, C. Arora, Sequestration of crystal violet from aqueous solution using ash of black turmeric rhizome, Desal. Water Treat., 220 (2021) 342–352.
[6] M. Kucukosmanoglu, O. Gezici, A. Ayar, The adsorption behaviors of methylene blue and methyl orange in a diaminoethane sporopolleninmediated column system, Sep. Purif. Technol., 52 (2006) 280–287.

[7] T.A. Saleh, V.K. Gupta, Photo-catalyzed degradation of hazardous dye methyl orange by use of a composite catalyst consisting of multi-walled carbon nanotubes and titanium dioxide, J. Colloid Interface Sci., 371 (2012) 101–106.
[8] K. Bhattacharya, A. Sharma, Kinetics and thermodynamics of methylene blue adsorption on neem (*Azadirachta indica*) leaf powder, Dyes Pigm., 65 (2005) 51–59.
[9] K.T. Chung, S.E. Stevens Jr., C.E. Cerniglia, The reduction of azo dyes by the intestinal microflora, Crit. Rev. Microbiol., 18 (1992) 175–190.
[10] K.T. Chung, The significance of azo-reduction in the mutagenesis and carcinogenesis of azo dyes, Mutat. Res., 114 (1983) 269–281.
[11] P.S. Kumar, M.J.S. Raja, M. Kumaresan, D.K. Loganathan, P.A. Chandrasekaran, New electrode reactor with in-built recirculation mode for the enhancement of methylene blue dye removal from the aqueous solution: comparison of adsorption, electrolysis, and combined effect, Korean J. Chem. Eng., 31 (2014) 276–283.
[12] D. Beqqour, G. Derouich, W. Taanaoui, A. Essate, M. Ouammou, S. Allami Younssi, J. Bennazha, J.A. Cody, M. El Rhazi, Development of composite ultrafiltration membrane made of PmPD/PVA layer deposited on ceramic pozzolan/micronized phosphate support and its application for Congo red dye removal, Desal. Water Treat., 240 (2021) 152–164.
[13] S. Dutta, B. Gupta, S.K. Srivastava, A.K. Gupta, Recent advances on the removal of dyes from wastewater using various adsorbents: a critical review, Mater. Adv., 2 (2021) 4497–4531.
[14] D.H.K. Reddy, K. Seshaiah, A.V.R. Reddy, S.M. Lee, Optimization of Cd(II), Cu(II), and Ni(II) biosorption by chemically modified *Moringa oleifera* leaves powder, Carbohydr. Polym., 88 (2012) 1077–1086.
[15] C. Arora, P. Kumar, S. Soni, J. Mittal, A. Mittal, B. Singh, Efficient removal of malachite green dye from aqueous solution using *Curcuma caesia* based activated carbon, Desal. Water Treat., 195 (2020) 341–352.
[16] S. Soni, P.K. Bajpai, D. Bharti, J. Mittal, C. Arora, Removal of crystal violet from aqueous solution using iron based metal organic framework, Desal. Water Treat., 205 (2020) 386–399.
[17] V.C. Patil, N.M. Rajeshwari, S. Samhita, S. Sthana, Vol. I, Chaukhamba Publications, New Delhi, 2018, pp. 400–401.
[18] C. Arora, S. Soni, S. Sahu, J. Mittal, P. Kumar, P.K. Bajpai, Iron based metal organic framework for efficient removal of methylene blue dye from industrial waste, J. Mol. Liq., 284 (2019) 343–352.
[19] M.S. Sajab, C.H. Chia, S. Zakaria, P.S. Khiew, Cationic and anionic modifications of oil palm empty fruit bunch fibers for the removal of dyes from aqueous solutions, Bioresour. Technol., 128 (2013) 571–577.
[20] P.S. Kumar, R. Sivaranjanee, U. Vinothini, M. Raghavi, K. Rajasekar, K. Ramakrishnan, Adsorption of dye onto raw and surface modified tamarind seeds: isotherms, process design, kinetics, and mechanism, Desal. Water Treat., 52 (2014) 2620–2633.
[21] X.-J. Liu, H.-Y. Zeng, S. Xu, C.-R. Chen, Z.-Q. Zhang, J.-Z. Du, Metal oxides as dual-functional adsorbents/catalysts for Cu^{2+}/Cr(VI) adsorption and methyl orange oxidation catalysis, J. Taiwan Inst. Chem. Eng., 60 (2016) 414–422.
[22] M. Makeswari, P. Saraswati, Photo catalytic degradation of methylene blue and methyl orange from aqueous solution using solar light onto chitosan bi-metal oxide composite, SN Appl. Sci., 2 (2020) 336, doi: 10.1007/s42452-020-1980-4.
[23] M. Adeel, M.S. Iltaf Khan, M. Muneer, N, Akra, Synthesis and characterization of Co–ZnO and evaluation of its photocatalytic activity for photodegradation of methyl orange, ACS Omega, 6 (2021) 1426–1435.
[24] M. Saeed, S. Adeel, H. Abdur-Raoof, M. Usman, A. Mansha, A. Ahmad, M. Amjed, ZnO catalyzed degradation of methyl orange in aqueous medium, Chiang Mai J. Sci., 44 (2017) 1646–1653.
[25] M. Tripathi, J.N. Sahu, P. Ganesan, Effect of process parameters on production of biochar from biomass waste through pyrolysis: a review, Renewable Sustainable Energy Rev., 55 (2016) 467–481.
[26] G. Lu, X. Lu, P. Liu, Reactivation of spent FCC catalyst by mixed acid leaching for efficient catalytic cracking, J. Ind. Eng. Chem., 92 (2020) 236–242.
[27] A. Mittal, J. Mittal, A. Malviya, V.K. Gupta, Adsorptive removal of hazardous anionic dye "Congo red" from waste water using waste materials and recovery by desorption, J. Colloid Interface Sci., 340 (2009) 16–26.
[28] B.S. Kaith, J. Sharma, S. Sethi, T. Kaur, U. Shankar, V. Jassal, Fabrication of green device for efficient capture of toxic methylene blue from industrial effluent based on $K_2Zn_3[Fe(CN)_6]_2{\cdot}9H_2O$ nanoparticles reinforced gum xanthanpsyllium hydrogel nanocomposite, J. Chin. Adv. Mater. Soc., 4 (2016) 249–268.
[29] U.A. Edet, A.O. Ifelebuegu, Kinetics, isotherms, and thermodynamic modeling of the adsorption of phosphates from model wastewater using recycled brick waste, Processes, 8 (2020) 665–680.
[30] K.Y. Foo, B. Hameed, Insights into the modeling of adsorption isotherm systems, Chem. Eng. J., 156 (2010) 2–10.
[31] A. Dada, A. Olalekan, A. Olatunya, O. Dada, Langmuir, Freundlich, Temkin and Dubinin–Radushkevich isotherms studies of equilibrium sorption of Zn^{2+} unto phosphoric acid modified rice husk, J. Appl. Chem., 3 (2012) 38–45.
[32] X. Yuan, W. Xia, J. An, J. Yin, X. Zhou, W. Yang, Kinetic and thermodynamic studies on the phosphate adsorption removal by dolomite mineral, J. Chem., 2015 (2015) 853105, doi: 10.1155/2015/853105.
[33] B. Armynah, D. Tahir, M. Tandilayuk, Z. Djafar, W.H. Piarah, Potentials of biochars derived from bamboo leaf biomass as energy sources: effect of temperature and time of heating, Int. J. Biomater., 2019 (2019) 3526145, doi: 10.1155/2019/3526145.
[34] V.K. Avornyo, A. Manu, D.A. Laird, M.L. Thompson, Temperature effects on properties of rice husk biochar and calcinated burkina phosphate rock, Agriculture, 11 (2021) 432, doi: 10.3390/agriculture11050432.
[35] Z. Ying, J.M.Z. He Ying, W. Daria, H. Fengxiang, R. Gaurab, T. Jinke, D. Qilin, Synthesis of Fe_2O_3/biochar nanocomposites by microwave method for magnetic energy-storage concentration cells, Mater. Lett.: X, 3 (2019) 100020, doi: 10.1016/j.mlblux.2019.100020.
[36] Z. Chen, F. Gao, K. Ren, Q. Wu, Y. Luo, H. Zhou, M. Zhang, Q. Xu, Mechanism of by-products formation in the isobutane/butene alkylation on HY zeolites, RSC Adv., 8 (2018) 3392–3398.
[37] Y. Sun, B. Gao, Y. Yao, J. Fang, M. Zhang, Y. Zhou, L. Yang, Effects of feedstock type, production method, and pyrolysis temperature on biochar and hydrochar properties, Chem. Eng. J., 240 (2014) 574–578.
[38] M. de C.E. Pinto, D.D. da Silva, A.L.A. Gomes, V. dos S.A. Leite, A.R.F. Moraes, R.F. de Novais, J. Tronto, F.G. Pinto, Film based on magnesium impregnated biochar/cellulose acetate for phosphorus adsorption from aqueous solution, RSC Adv., 9 (2019) 5620–5627.
[39] T.M. Salamaa, I.O. Ali, A.I. Hanafya, W.M. Al-Meligy, A novel synthesis of NaA zeolite encapsulated iron(III) Schiff base complex: photocatalytic oxidation of direct blue-1 dye with hydrogen peroxide, Mater. Chem. Phys., 113 (2009) 159–165.
[40] Z. Anfar, M. Zbair, H.A. Ahsiane, J. de Amane, N. El Alem, Microwave-assisted green synthesis of Fe_2O_3/biochar for ultrasonic removal of nonsteroidal anti-inflammatory pharmaceuticals, RSC Adv., 10 (2020) 11371–11380.
[41] S. Xia, K. Li, H. Xiao, N. Cai, Z. Dong, C. Xu, Y. Chen, H. Yang, X. Tu, Pyrolysis of Chinese chestnut shells: effects of temperature and Fe presence on product composition, Bioresour. Technol., 287 (2019) 121444, doi: 10.1016/j.biortech.2019.121444.
[42] D. Shan, S. Deng, T. Zhao, B. Wang, Y. Wang, J. Huang, G. Yu, J. Winglee, M.R. Wiesner, Preparation of ultrafine magnetic biochar and activated carbon for pharmaceutical adsorption and subsequent degradation by ball milling, J. Hazard. Mater., 305 (2016) 156–163.

[43] D. Ozturk, T. Şahan, E. Dişli, N. Aktaş, Optimization with response surface methodology (RSM) of adsorption conditions of Cd(II) ions from aqueous solutions by pumice, Hacettepe J. Biol. Chem., 42 (2014) 183–192.
[44] H.J. Rao, P. King, Y.P. Kumar, Application of response surface methodology for optimization of cadmium adsorption in an aqueous solution by activated carbon prepared from *Bauhinia purpurea* leaves, Rasayan J. Chem., 11 (2018) 1577–1586.
[45] T.T. Shumba, M. Tapera, J. Mumbi, Biochar versus iron oxide-biochar performance as adsorbents for lead and methyl orange from an aqueous solution, J. Mater. Sci. Res. Rev., 4 (2019) 1–12.
[46] N. Chaukura, E.C. Murimba, W. Gwenzi, Synthesis, characterisation and methyl orange adsorption capacity of ferric oxide–biochar nano-composites derived from pulp and paper sludge, Appl. Water Sci., 7 (2017) 2175–2186.
[47] F.Z. Addar, S. El-Ghzizel, M. Tahaikt, M. Belfaquir, M. Taky, A. Elmidaoui, Fluoride removal by nanofiltration experimentation, modelling and prediction based on the surface response method, Desal. Water Treat., 240 (2021) 75–88.
[48] A. Karami, K. Karimyan, R. Davoodi, M. Karimaei, K. Sharafie, S. Rahimi, T. Khosravi, M. Miri, H. Sharafi, A. Azari, Application of response surface methodology for statistical analysis, modeling, and optimization of malachite green removal from aqueous solutions by manganese-modified pumice adsorbent, Desal. Water Treat., 89 (2017) 150–161.
[49] S. Soni, P.K. Bajpai, D. Bharti, J. Mittal, C. Arora, Removal of crystal violet from aqueous solution using iron based metal organic framework, Desal. Water Treat., 205 (2020) 386–399.
[50] O.I. Kingsley, J.O. Ighalo, E.C. Emenike, L.A. Ogunfowora, C.A. Igwegbe, Adsorption of methyl orange: a review on adsorbent performance, Curr. Res. Green Sustainable Chem., 4 (2021) 100179, doi: 10.1016/j.crgsc.2021.100179.
[51] X. Shenghui, P. Huang, J.J. Kruzic, X. Zeng, H. Qian, A highly efficient degradation mechanism of methyl orange using Fe-based metallic glass powders, Sci. Rep., 6 (2016) 21947, doi: 10.1038/srep21947.
[52] M.-H. Baek, C.O. Ijagbemi, D.-S. Kim, Removal of malachite green from aqueous solution using degreased coffee bean, J. Hazard. Mater., 176 (2010) 820–828.
[53] B.H. Hameed, M.I. El-Khaiary, Batch removal of malachite green from aqueous solutions by adsorption on oil palm trunk fibre: equilibrium isotherms and kinetic studies, J. Hazard. Mater., 154 (2008) 237–244.
[54] R. Malik, D.S. Ramteke, S.R. Wate, Adsorption of malachite green on groundnut shell waste based powdered activated carbon, Waste Manage., 27 (2007) 1129–1138.
[55] J. Chen, X. Shi, Y. Zhan, X. Qiu, Y. Du, H. Deng, Construction of horizontal sstratum landform-like composite foams and their methyl orange adsorption capacity, Appl. Surf. Sci., 397 (2017) 133–143.
[56] Z. Zhou, R. Liu, Fe_3O_4@polydopamine and derived Fe_3O_4@ carbon core–shell nanoparticles: comparison in adsorption for cationic and anionic dyes, Colloids Surf., A, 522 (2017) 260–265.